Supporting Information

Ultrathin single-ion sieving membrane with sub-1-nm channels for suppressing Li dendrite and polysulfide shuttling

Rongrong Li[1,3], Yichi Wang[1,5], Jingmin Zhang[1,4], Jun Yang[1], Jiang He[1,4]*, Wenjie Mai[1,2]*, Xiong Pu[1,4]*

[1] CAS Center for Excellence in Nanoscience, Beijing Key Laboratory of Micro-Nano Energy and Sensor, Beijing Institute of Nanoenergy and Nanosystems, Chinese Academy of Sciences, Beijing 101400, China

[2] Siyuan Laboratory, Guangdong Provincial Engineering Technology Research Center of Vacuum Coating Technologies and New Energy Materials, Department of Physics, Jinan University, Guangzhou 510632, Guangdong, China

[3] School of Physical Science, University of Chinese Academy of Sciences, Beijing 101408, China.

[4] School of Nanoscience and Technology, University of Chinese Academy of Sciences, Beijing 100049, China.

[5] Beijing National Center for Electron Microscopy and Laboratory of Advanced Materials, School of Materials Science and Engineering, Tsinghua University, Beijing, 100084, China.

*E-mail: hejiang@binn.cas.cn; wenjiemai@email.jnu.edu.cn; puxiong@binn.cas.cn

List of content

1. Supplmentary Experimental Methods

1.1 Experimental reagents.

1.2 Preparation of separators.

1.3 Synthesis of sulfur cathodes.

1.4 Materials characterizations.

1.5 Permeation measurements.

1.6 Electrochemical measurements.

1.7 Finite element simulations.

1.8 Molecular Dynamics.

1.9 Li-S pouch cell testing.

2. Supplmentary Figures (1−27)

1. The synthesis process of GP/HPP membrane.

2. The optical photograph of as-prepared GP/HPP separator.

3. The FTIR spectra of bare PP, hydrophilic HPP, and GP-HPP separators.

4. The Raman spectra of PP, HPP, GO/HPP and GP/HPP separators, respectively.

5. The high-resolution XPS spectra of C 1s.

6. The SEM images of PP and HPP separators.

7. The repeatedly bending and wrinkling tests of GP/HPP membrane.

8. The tensile test of PP, HPP, and GP/HPP membranes.

9. The SEM images of films with different filtrated volumes.

10. The AFM measurements of GP/HPP membrane with different regions.

11. The XRD patterns of HPP, GO/HPP, and GP/HPP separators, respectively.

12. The comparing XRD data of GP/HPP and GO/HPP membranes before and after soaking in DOL/DME solvent.

13. The visual penetration experiment in H-type installations with HPP, GP/HPP-4.0 mL (40% PDA content) membranes.

14. The optical photograph of GP/HPP-4.0 mL (10%) membrane after penetration

experiment.

15. Nyquist plots of PP, HPP, and GP/HPP separators estimating the ionic conductivity.

16. Chronoamperometry measurements of symmetric Li‖Li cell at 10 mV of polarization and the Nyquist plots before and after polarization with different membranes.

17. Comparison of Li^+ transfer number for GP/HPP and other reported sieving membranes

18. Molecular snapshots of Li^+ ion at different locations of GP/HPP membranes during the transport process.

19. Molecular snapshots of S_6^{2-} ion at different locations of GP/HPP membranes during the transport process.

20. The charge/discharge curves of membranes at low current density.

21. Polysulfide permeation measurements in H-type cells with different separators.

22. The shuttle current tests of PP and GP/HPP-1.0 mL separators.

23. Voltage-time profiles of symmetric Li‖Li cell with PP and GP/HPP membranes.

24. The profiles of Li plating/stripping processes in asymmetric Li‖Cu cells.

25. Finite element simulations explore the influence of GP/HPP membrane on tuning the distribution of electric potential and the current density.

26. Comparison of the corresponding plating/stripping voltage profiles of Li‖Cu half cells with GP/HPP and PP separators.

27. The cross-sectional SEM images comparing the lithium deposited thickness of GP/HPP and PP membranes.

28. Thermogravimetric profiles of Super P-C/S composite.

29. The charge/discharge curves of cells with PP separator at various current densities.

30. The investigations of Li^+ diffusion coefficient (D_{Li+}) based on GP/HPP and PP separators.

31. The optical photograph and SEM image of GP/HPP after the long-term cycling.

32. The charge/discharge curves at different cycle numbers of Li-S pouch cells.

33. The optical photographs of Li-S pouch cells power LED arrays with GP/HPP and PP separator.

3. Supplementary References (1-20)

1. Supplementary Experimental Methods

1.1 Experimental reagents.

GO nanosheets were prepared according to a previous literature method, including the process of expansion, pre-oxidation, and oxidation.[1] Dopamine hydrochloride (DA-HCl), ammonium hydroxide, sublimed sulfur, and methyl alcohol were purchased from Shanghai Aladdin. The commercial conductive carbon (Super P) was purchased from HF-Kejing. These reagents were used without further pretreatment.

1.2 Preparation of separators.

Preparation of hydrophilic polypropylene separator (HPP): The hydrophilic modification of PP (Celgard 2500) separator was achieved by using dopamine treatment. The trimmed PP membrane was immersed in methanol aqueous solution (100 mL, methanol: water = 1:1 by vol) for 12 h. The prepared DA-HCl solution (0.25 M 10 mL) was poured into the above methanol solution, then the appropriate amount of ammonia was dropped until the value of pH$\geq$8.5. The color of this solution altered from colorless to black. After reacting for 24 h, the treated PP separation was fetched out, rinsed several times with deionized water, and preserved in water.

Preparation of GO-PDA dispersion: The as-prepared GO powder (2.2 g) was dispersed in 1000 mL deionized water with vigorous stirring for 12 h to obtain a homogeneous GO aqueous solution (2.2 mg/mL). 22.7 mL of GO solution (2.2 mg/mL) was dispersed in 67.3 mL DI water, then mixed with 10 mL DA-HCl solution (0.5 mg/mL) under magnetic stirring for 12 h. The pH of above mixed solution was adjusted to 8.5 by using ammonium hydroxide. After polymerization, the 0.5 mg/mL GO-PDA dispersion was obtained (GO: PDA = 100:10 by mass). The 0.5 mg/mL GO-PDA dispersion with the ratio of 100:40 was prepared using a similar method and pure 0.5 mg/mL GO dispersion was also obtained without adding DA-HCl solution.

Preparation of uniform GP/HPP separator: The different GP/HPP separator was prepared by vacuum filtration of the dilute GO-PDA dispersion through the HPP membrane as a filter. Different volumes (range from 0.4 to 10 mL) of the as-prepared 0.5 mg/mL GO-PDA dispersion were diluted at a ratio of 1:10 (by vol) and filtered under vacuum, then dried at 60 °C for 12 h. Using diluted process and repeatedly

washed the GP/HPP separator with DI water could remove the free PDA particles effectively.

1.3 Synthesis of sulfur cathodes.

Commercial Super P and sublimed sulfur (S) were mixed at a ratio of 1:4 (by mass) and ground for 15 min to form a uniform mixture. This powder was heated at 155 °C for 12 h with rate of 1 °C/min under an Ar atmosphere. Then the sulfur composites (C/S) were obtained. Sulfur cathodes were prepared by mixing 80 wt.% as-prepared C/S, 10 wt.% Super P, and 10 wt.% polyvinyldifluoride (PVDF as a binder) with N-methyl-2-pyrrolidone (NMP as a dispersant) to form a ropy slurry. The slurry was coated onto a carbon paper substrate, followed by drying at 60 °C for 12 h. The sulfur cathodes were obtained by punching the substrate into 12 mm diameter disks, with a sulfur loading of about 1.4-3.4 mg/cm^2.

1.4 Materials characterizations.

The morphology and structure of separators were analyzed by scanning electron microscopy (SEM) and transmission electron microscopy (TEM) images were taken on a Nova NanoSEM 450 and Tecnai G2 F20 S-TWIN TMP systems, respectively. Atomic force microscopy (AFM) images were observed by MFP-3D-SA, with the sample prepared by coating from diluted aqueous solution onto a plasma-cleaned silicon wafer. XRD data were performed on the Xpert3 Powder instrument using Cu Kα radiation (λ=1.5418 Å). The surface chemical compositions of prepared membranes were collected by using the Themo Scientific K-Alpha X-ray spectrophotometer (XPS) with Al Kα radiation. The chemical bonds of samples were recorded by using Fourier transform infrared (FT-IR, VERTEX80v) spectra. Raman spectra were measured using a LABRAM HR EVOLUTION equipment with a 514 nm excitation laser. The zeta potentials of GO and GO-PDA powder were measured using a Zetasizer Nano-ZS ZEN3600. The content of sulfur was obtained by using a thermogravimetric analysis (TG) test.

1.5 Permeation measurements.

To approximate the actual working battery environment, a lithium polysulfide (LiPS) solution was prepared by dissolving sublimed sulfur and lithium metal into the

electrolyte (1,2-dimethoxyethane (DME): 1,3-dioxacyclopentane (DOL)=1:1, v/v, with 2 wt.% $LiNO_3$). To meet the experimental requirements, the above saturated LiPS solution should be further diluted at a ratio of 1:10 (by vol). Then, this LiPS solution was added to one side of the U-shaped glass bottles. The other side was filled with electrolyte without LiPSs. The two vessels were intercepted by as-prepared GP/HPP, GO/HPP, HPP membranes, and the pure PP separator, respectively.

1.6 Electrochemical measurements.

Ionic conductivity: The ionic conductivities (σ) of pure PP, HPP, and GP/HPP separators were measured through electrochemical impedance spectroscopy (EIS) analyses. The separator was sandwiched between two stainless steels in coin-type cells (CR 2032) with ample electrolyte. The EIS tests were measured using a CHI760E electrochemical workstation (Shanghai Chenhua Instrument Co., LTD) with a frequency range of 0.1-100 kHz under Open Circuit Potential (OCP). The ionic conductivity was obtained according to the following equation:

$$\sigma = \frac{l}{AR_b}$$

where σ is the ionic conductivity (S/cm), l is the thickness of the membrane (cm), A represents the area of the stainless-steel electrode (cm^2), and R_b stands for the bulk resistance (Ω), respectively.

Li-ion transfer number: The lithium-ion (Li^+) transfer number (t_{Li+}) of pure PP, HPP, and GP/HPP separators were measured with chronoamperometry at a constant step potential of 10 mV. The separator was sandwiched between two lithium metal electrodes in coin-type cells (CR 2032) with ample electrolyte. The t_{Li+} was calculated according to the following equation:

$$t_{Li^+} = \frac{I_s(\Delta V - I_0 R_0)}{I_0(\Delta V - I_s R_s)}$$

where t_{Li+} is the Li-ion transfer number, I_s and I_0 is the steady-state and initial current (mA), R_o and R_s stand for the bulk resistance (Ω), and ΔV is the constant potential (=10 mV), respectively.

Electrochemical testing of lithium plating/stripping: To investigate the effect of the separator on lithium metal anode, the symmetric Li//Li and asymmetric Li//Cu cells were assembled with Li-S electrolyte. For the Li electrode, the diameter and thickness were 10.0 mm and 0.5 mm, respectively. These studies were conducted on Neware battery testers at 27 °C. For the ex-situ SEM test, the cells were disassembled in an Ar-filled glove box and washed by DME.

Electrochemical testing of Li-S coin-type cells: Coin-type cells were assembled in an Ar-filled glove box using Super P@S cathodes, Li metal anodes (diameter: 16 mm, thickness: 0.5 mm) and as-prepared functional separators. The electrolyte of cells was DME: DOL=1:1, v/v, with 2 wt.% $LiNO_3$ and 1 M LiTFSI. The consumption of electrolyte is 40 μL in coin cells. The cyclic voltammetry (CV) curves were carried out using a CHI760E electrochemical workstation in the voltage range from 1.8 to 3.0 V at 0.1 mV/s. The Li^+ diffusion coefficient was evaluated through CV testing at different scan rates from 0.1-0.5 mV/s. The EIS tests were measured with a frequency range of 0.1-100 kHz. All galvanostatic discharge/charge profiles (1.8-3.0 V) were conducted on the Neware (Shenzhen) battery test station at 27 °C.

Shuttling current test: The Li-S coin-type cells were assembled in Ar-filled glove box without $LiNO_3$ additive. These cells were pre-cycled for three cycles at 0.5 C (1 C=1672 mA/g) to form stable SEI. Then, discharged to 2.38 V and switched to potentiostatic mode for 15 000 s to measure the shuttling current.

1.7 Finite element simulations.

COMSOL Multiphysics was carried out to the distribution of electric field, local current density, and the concentration of Li^+ at the lithium deposition interface. According to the SEM and TEM characterizations of the GP/HPP membrane, the geometric model of membrane is built with a thickness of 60 nm, which presents a layered structure distribution. The interlayer distance of this model was set as 1 nm. The ultra-thin films were confined in the bulk electrolyte. The initial concentration of electrolyte is 1 M. The current density of upper boundary was set to 2.5 mA/cm^2 and the Li-ion diffusion coefficient is 1×10^{-9} m^2/s according to the ref.[2]. The current density in an electric field is described by continuity equation:

$$i = -F \sum -z_i^2 m_i F c_i \nabla \emptyset_i$$

Where i is the current density (A/m^2), z_i is the charge number, m_i is ionic mobility (mol·m^2·s·V·A), F represents the Faraday's constant (A·s/mol), $\emptyset_i$ is ionic potential, and c_i is ion concentration. At the same time, the current density conservation should be satisfied:

$$\nabla \cdot i = 0$$

The electrochemical reaction on the surface of electrodes is realized by Butler–Volmer equation:

$$i_a = i_0 \left(\frac{c}{c_0} exp(\eta(1-\beta)F/(RT)) - exp(\eta\beta F/(RT)) \right)$$

Herein, i$_a$ is the local current density, i$_0$ is the exchange current density, η is the overpotential, β is the transfer coefficients, c and c_0 denotes the concentration of reduced species and oxidized species, F represents the Faraday's constant, R is the ideal gas constant, and T is the operating temperature. The transport of ions can be described according to Fick's law:

$$-D\nabla C - zmFc\nabla\emptyset_l = N$$

Where C is ion concentration, z is the valence, D is the diffusion coefficient, m is ionic mobility, F represents Faraday's constant, $\emptyset_l$ is ionic potential.

1.8 Molecular Dynamics.

Molecular Dynamics (MD) simulations of the crossing process of Li$^+$ and S$_6^{2-}$ through the PDA/GO composite membrane were performed using Gromacs program suite. The OPLS-AA force field[3] was used to describe the GO, DE, DOL, and PDA molecules. The TFSI anion and lithium cation were parameterized using CL&P force field[4]. All these topology files of these molecules were generated directly using AuToFF web server[5].

These simulations were carried out at a pressure of 1.01325×10^5 Pa using the Berendsen's barostat[6] with a semi-thermal compressibility constant of 4.5×10^{-5}. Velocity-rescale thermostat[7] with a relaxation constant of 1 ps was used to control the temperature at 298.15 K. Periodic boundary conditions were applied in all directions.

Particle-mesh Ewald (PME) method[8] with a cut-off distance of 15 Å was applied to treat the electrostatic interactions and the van der Waals forces. All bonds involving hydrogen atoms were constrained with the LINCS algorithm.

There are forty configurations for umbrella sampling generated by pulling the Li^+ and S_6^{2-} through the membrane system along the Z-axis using steered molecular dynamics simulations. Each configuration was then performed an additional 1 ns equilibrium process at constant NPT ensemble with the same simulation parameters as above. After the system pressure has reached an equilibrium, 5 ns molecular dynamics sampling was performed for next calculation of free energy profiles through weighted histogram analysis method (WHAM).

1.9 Li-S pouch cell testing.

The Li-S pouch cells were assembled in an Ar-filled gloved box using Al-plastic films (4 cm by 5 cm) as package materials. Cathodes were prepared by mixing as-prepared C/S, Super P, and PVDF binder with a mass ratio of 8:1:1 in NMP dispersant to form a slurry. The resulting slurry was coated onto a carbon paper current collector (2 cm by 2 cm), followed by drying at 60 °C overnight. The sulfur loading of cathode is as high as 17 mg. A piece of Li foil (3 cm by 3 cm) was tailored with a thickness is 0.5 mm. The amount of lithium anodes is excessive, resulting in the value of N/P being high. Al tabs and Ni tabs were riveted on the carbon papers and Li foils, respectively. GP/HPP and PP separator were stacked on the surface of the sulfur cathodes, respectively. The Li foil was put on the top of separator. Then, the stacked layers were inserted into the Al-plastic pocket. Finally, 0.5 mL of electrolyte was injected into this pocket and sealed under vacuum to get pouch cells with GP/HPP and PP separator.

2. Supplementary Figures
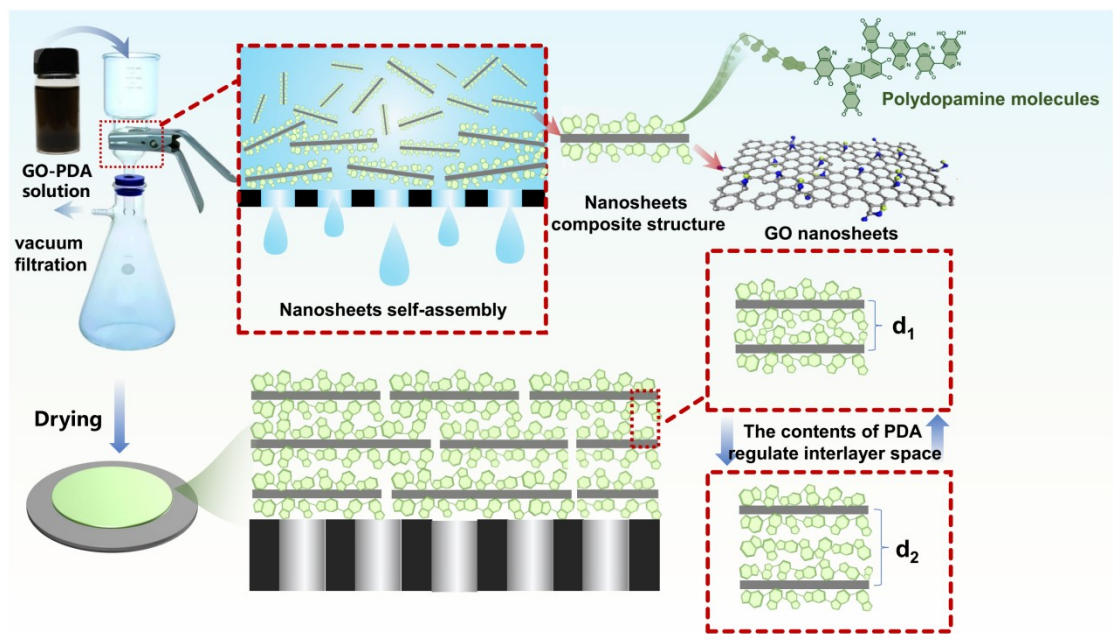
Supplementary Figure 1. The synthesis process of GP/HPP membrane with different thicknesses and regulated interlayer spacings.
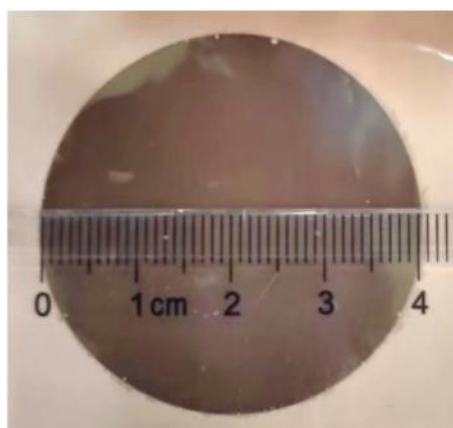
Supplementary Figure 2. The optical photograph of as-prepared GP/HPP separator.
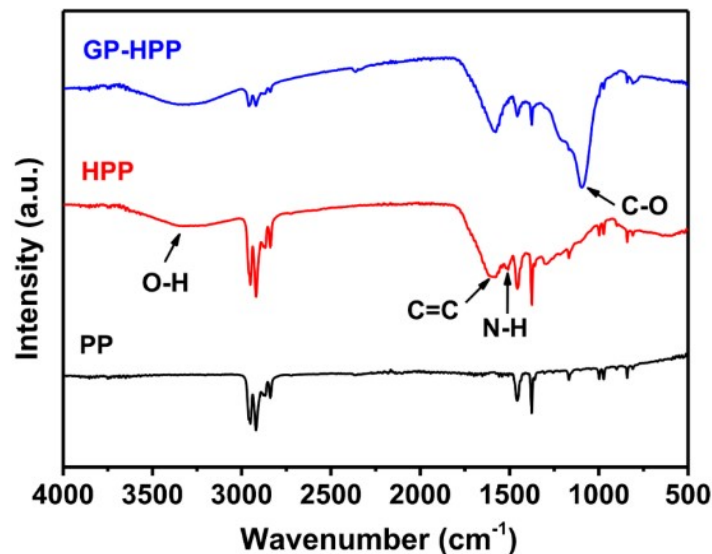
Supplementary Figure 3. The FTIR spectra of bare PP, hydrophilic HPP, and GP-HPP separators.

The broad peak at around 3300 cm^{-1} represents the O-H/N-H stretching vibration of the hydroxyl/amide groups in PDA[9], while the bonds centered at 1589 cm^{-1} and 1512 cm^{-1} are attributed to C=C stretching and N-H bending vibration, respectively[10]. In the GP/HPP spectrum, the sharp peak at 1095 cm^{-1} should be attributed to the C-O bending in GO nanosheets[11]. The results demonstrate the presence of electronegative oxygen-containing functional groups in the GP/HPP membrane. Additionally, the bond of N-H in PDA disappeared in GP/HPP sample, which should be ascribed to the formation of amide bond between N-H group and -COOH group of GO[9]. Although the -C=O bonds would be reduced to -C-O groups by the released electrons during oxidative polymerization of catecholeamines in poly-(dopamine) molecules, this is solid evidence supporting the covalently interaction of PDA and GO[11].
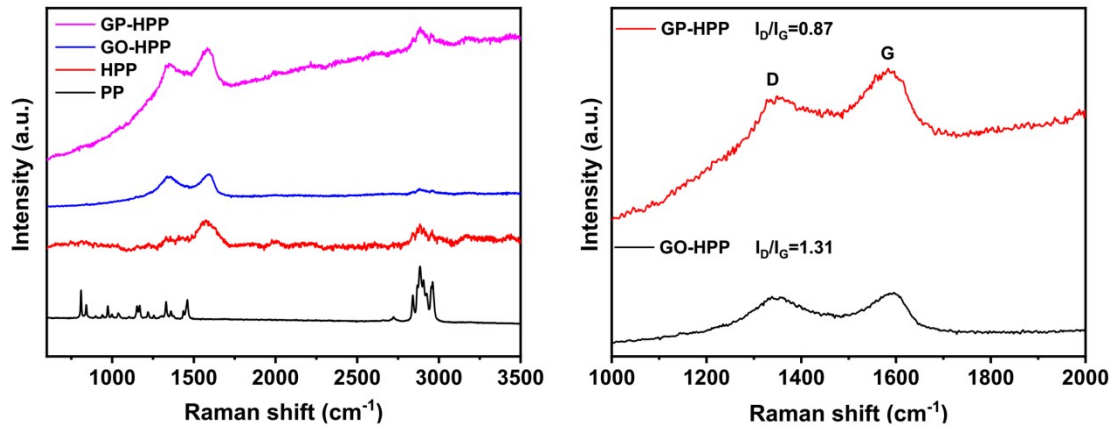
Supplementary Figure 4. The Raman spectra of PP, HPP, GO/HPP and GP/HPP separators, respectively.
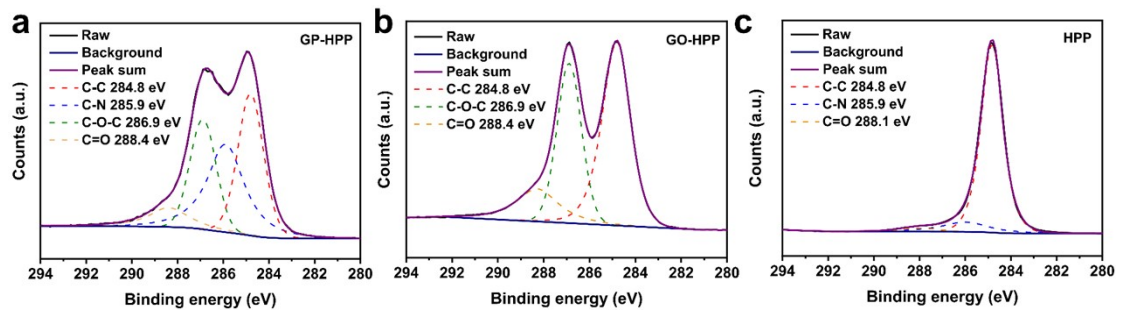
Supplementary Figure 5. The high-resolution XPS spectra of C 1s. The peaks at 284.8, 285.9, 286.9, and 288.4 (288.1) eV correspond to C-C, C-N, C-O-C, and C=O bonds, respectively[12].
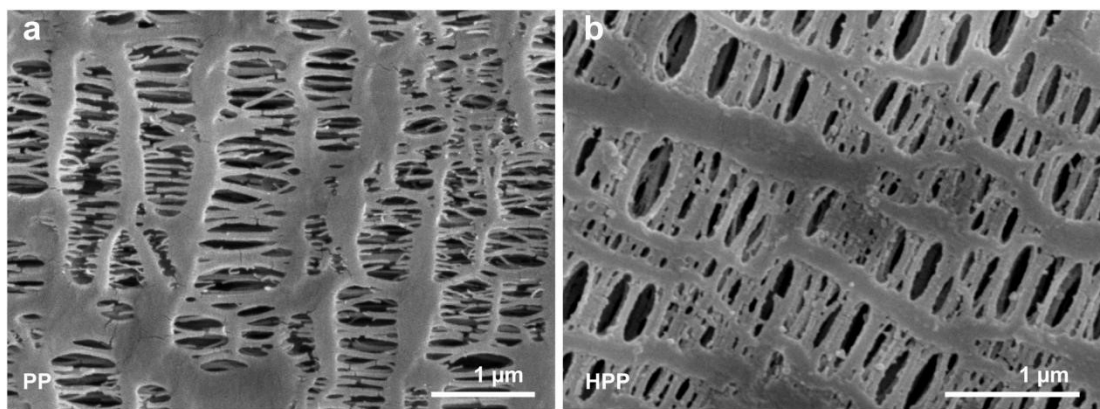
Supplementary Figure 6. The SEM images of PP and HPP separators.
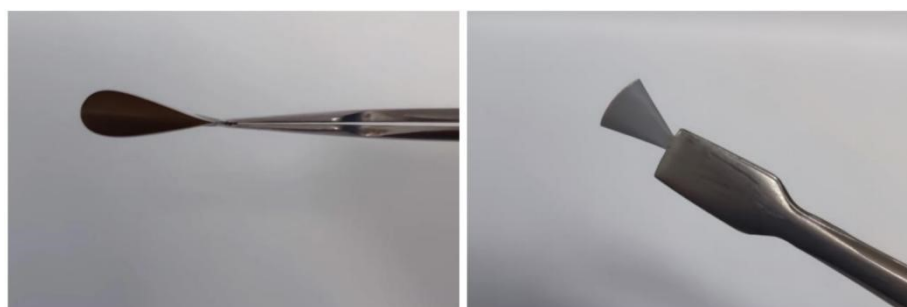
Supplementary Figure 7. The repeatedly bending and wrinkling tests of GP/HPP membrane.
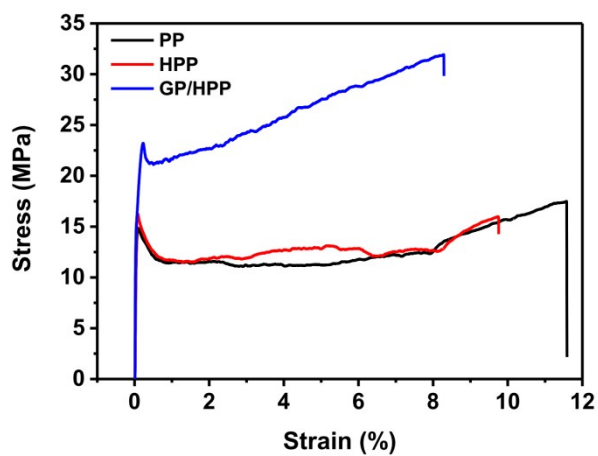
Supplementary Figure 8. The tensile test of PP, HPP, and GP/HPP membranes.
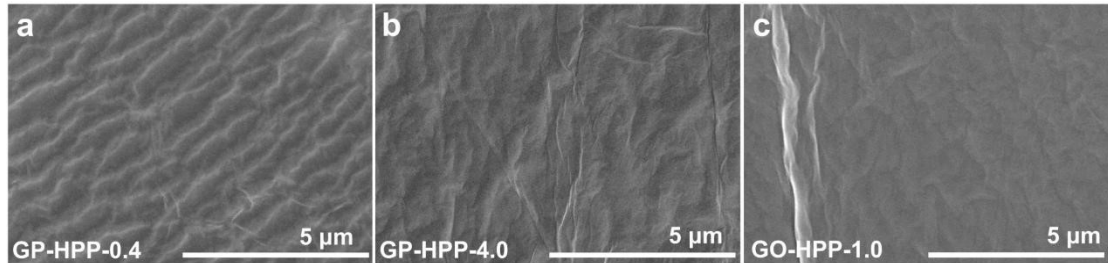
Supplementary Figure 9. (a, b) The SEM images of GP/HPP films with different filtrated volumes and (c) the GO/HPP film.
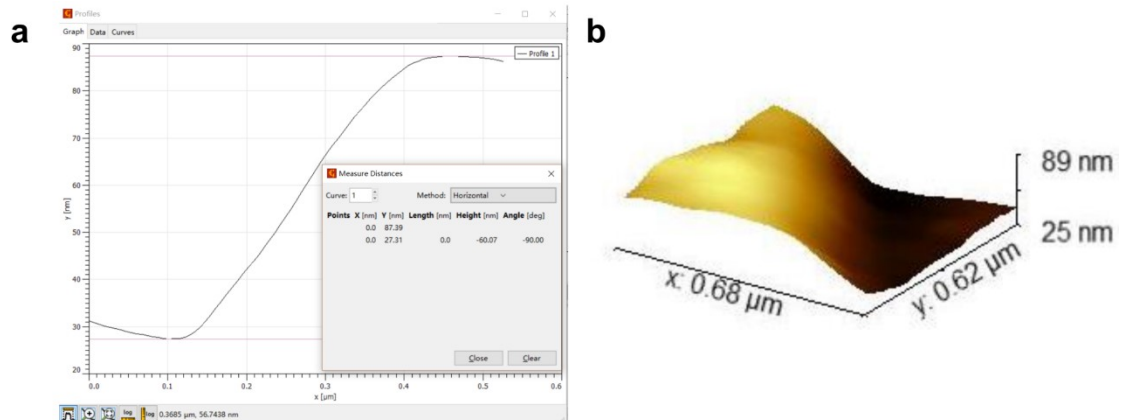
Supplementary Figure 10. The AFM measurements of GP/HPP membrane with different regions.
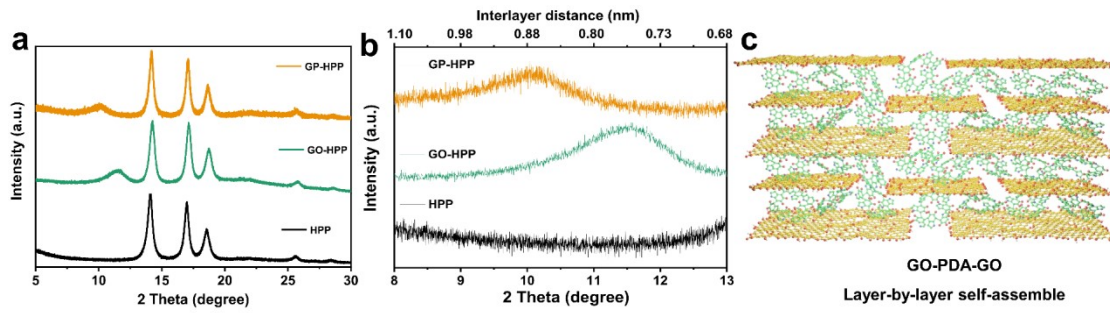
Supplementary Figure 11. (a) The XRD patterns of HPP, GO/HPP, and GP/HPP separators, respectively. The diffraction peaks at degree range from 8 to 13° is the corresponding interlayer distances; (b) The interlayer distances of HPP, GO/HPP, and GP/HPP separators, respectively; (c) Schematic illustration along with the TEM images and XRD pattern of a typical interlayer structure of GO-PDA film showing the layer-by-layer graphene-supported ion channel.
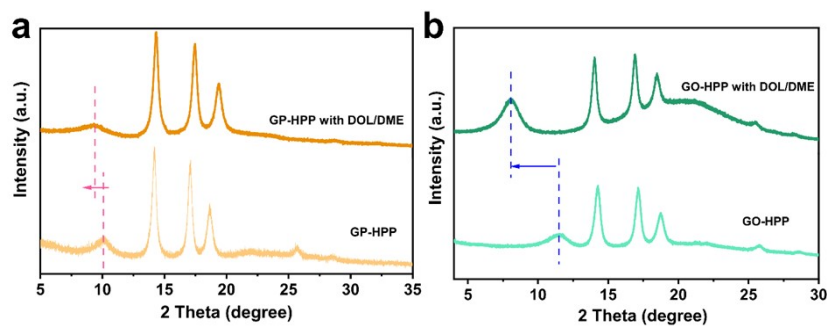
Supplementary Figure 12. The comparing XRD data of GP/HPP and GO/HPP membranes before and after soaking in DOL/DME solvent.
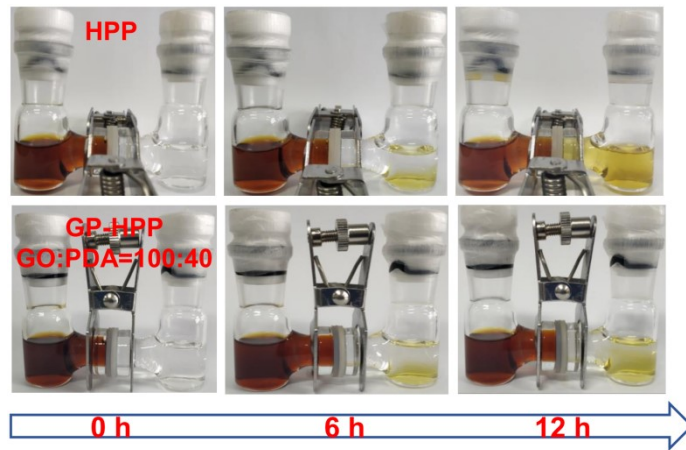
Supplementary Figure 13. The visual penetration experiment in H-type installations with HPP and GP/HPP-4.0 mL with 40% PDA content.
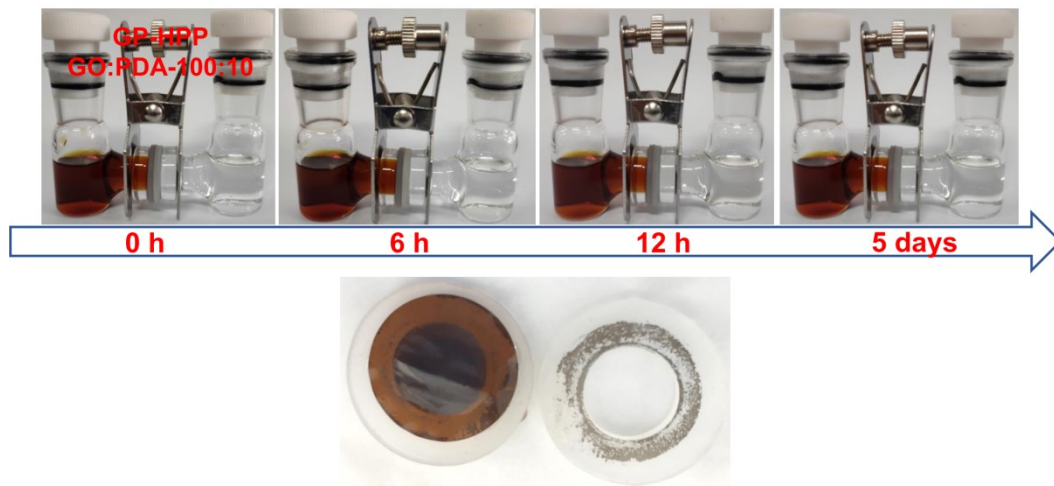
Supplementary Figure 14. The visual penetration experiment of GP/HPP-4.0 mL with 10% PDA content and its optical photograph after immersion in the electrolyte for 5 days.
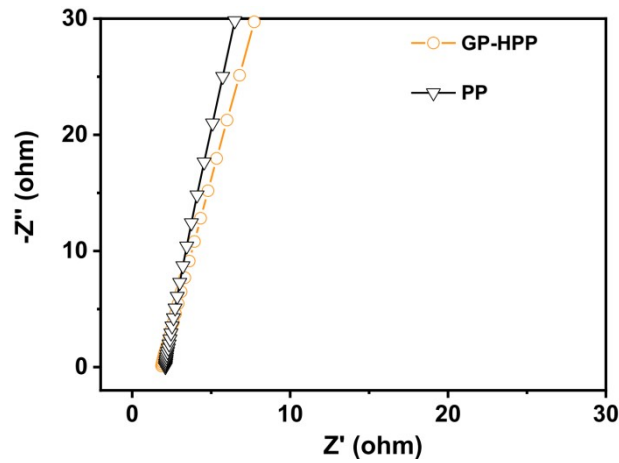
Supplementary Figure 15. Nyquist plots of PP and GP/HPP (100:10, 1.0 mL) separators for estimating the ionic conductivity.
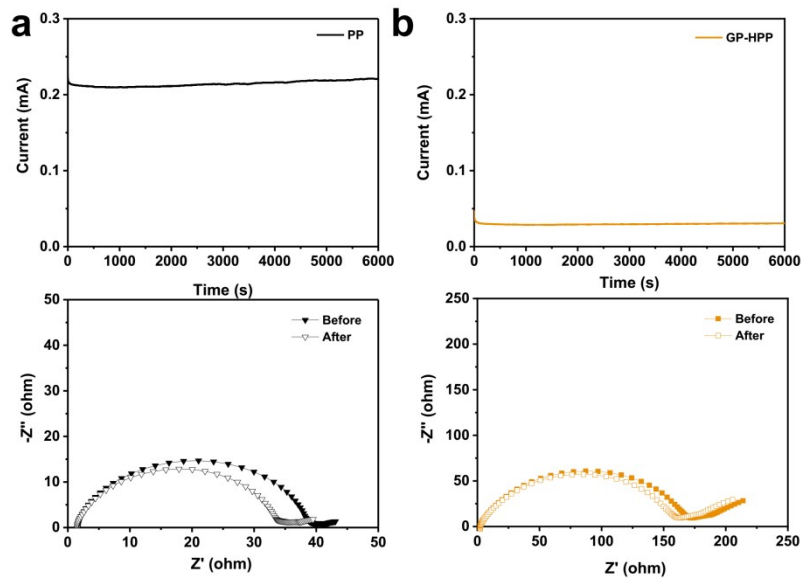

Supplementary Figure 16. i-t curves and Nyquist plots of PP and GP/HPP (100:10, 1.0 mL) separators for estimating the transfer number of Li-ion.
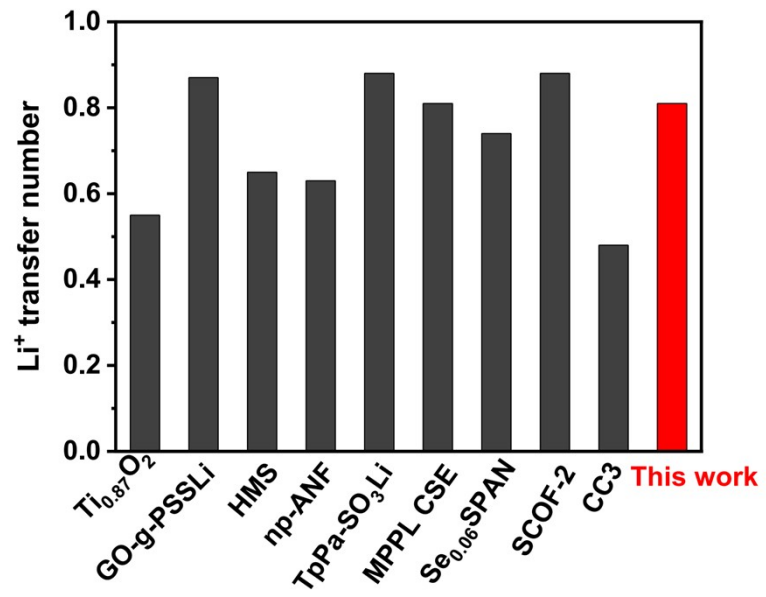
Supplementary Figure 17. Comparison of Li$^+$ transfer number for GP/HPP and other reported sieving membranes[2,13-20].
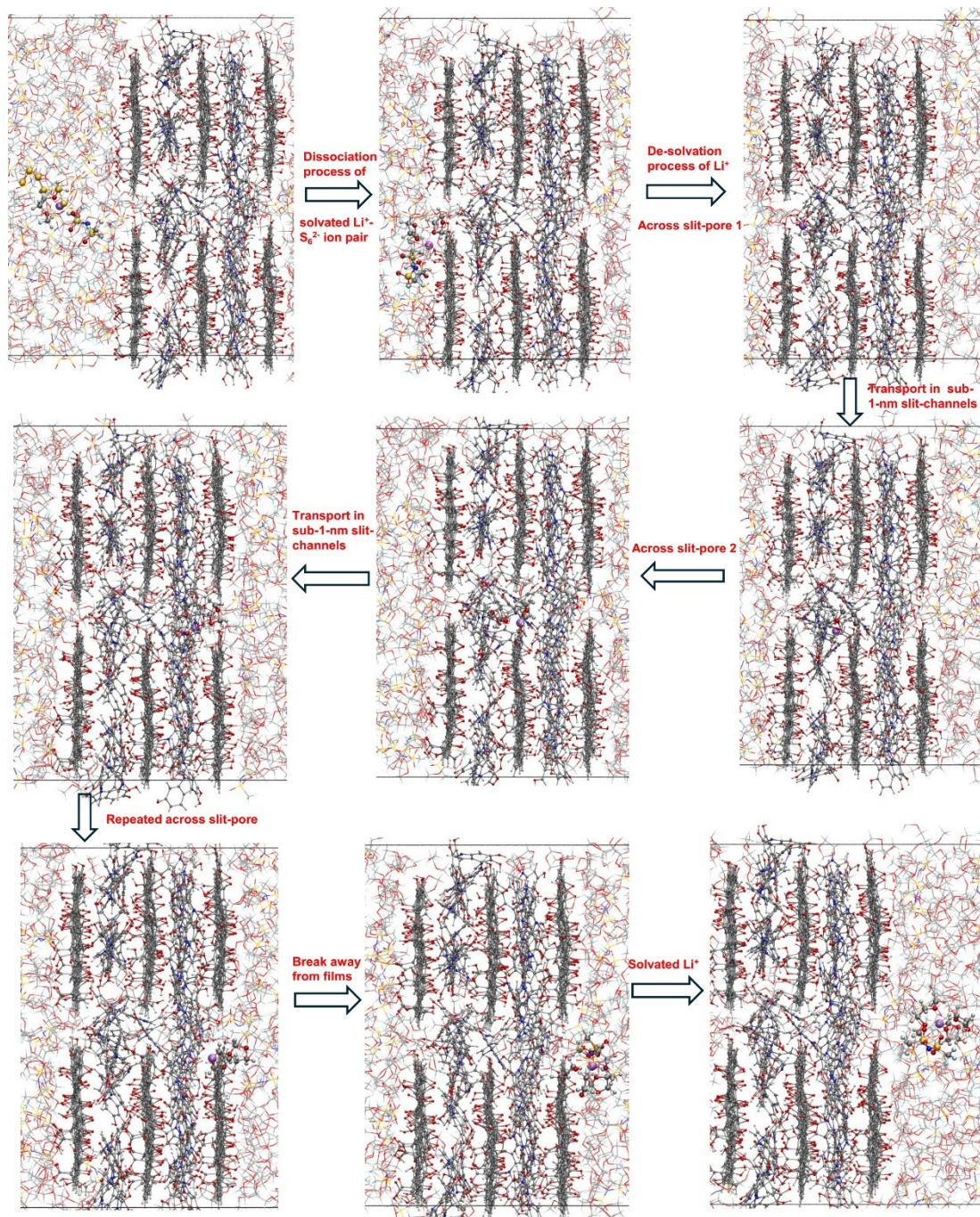
Supplementary Figure 18. Molecular snapshots of Li$^+$ ion at different locations of GP/HPP membranes during the transport process.
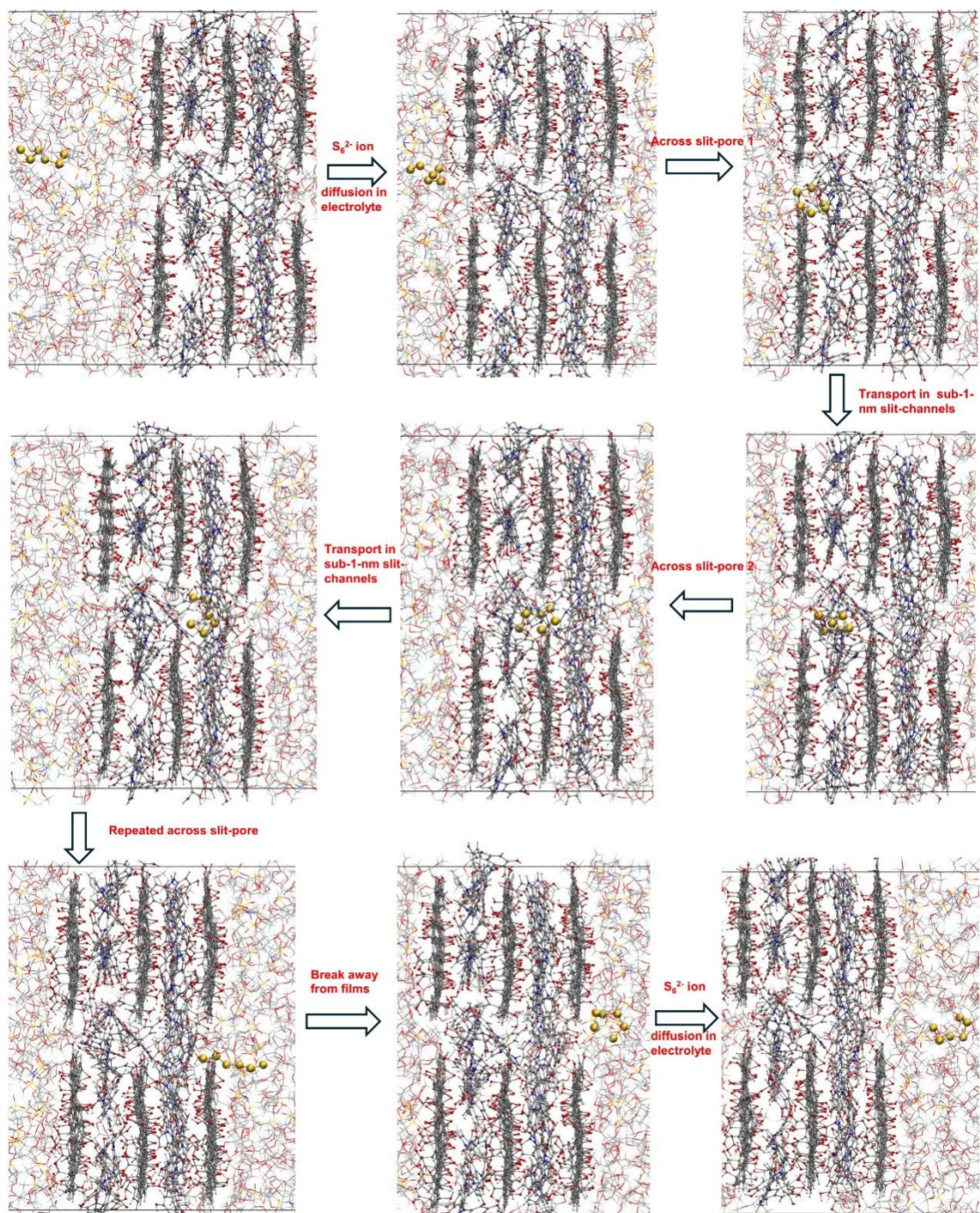
Supplementary Figure 19. Molecular snapshots of S_6^{2-} ion at different locations of GP/HPP membranes during the transport process.
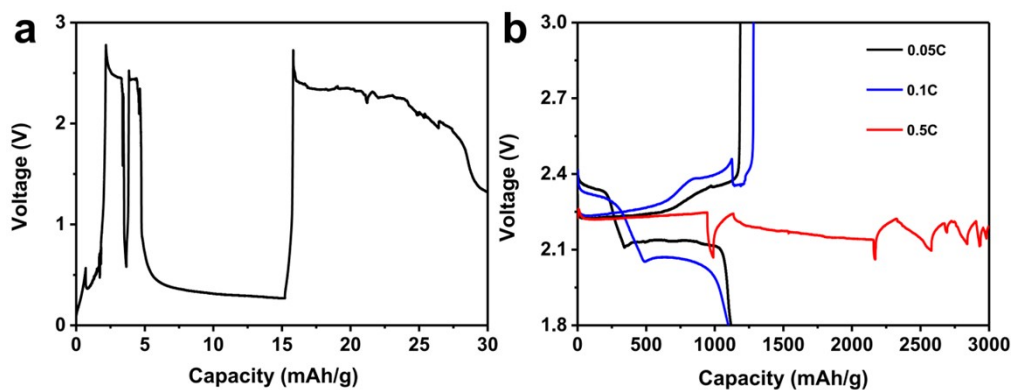
Supplementary Figure 20. The charge/discharge curves of (a) GP/HPP-4.0 mL membrane at 0.05 C, (b) GP/HPP-2.0 mL at the rate of 0.05 C, 0.1 C, and 0.5 C, respectively, where 4.0 and 2.0 mL represent the filtration volume of GO-PDA suspension.
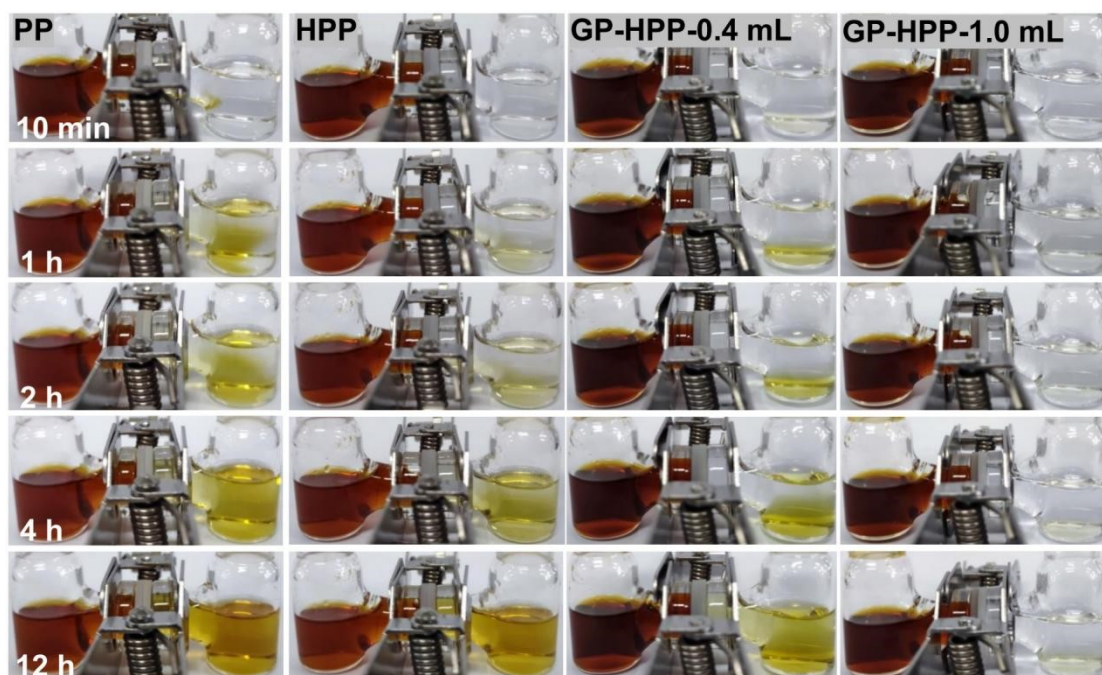

Supplementary Figure 21. Polysulfide permeation measurements in H-type cells with bare PP, HPP, GP/HPP-0.4 mL, and GP/HPP-1.0 mL separators, respectively.
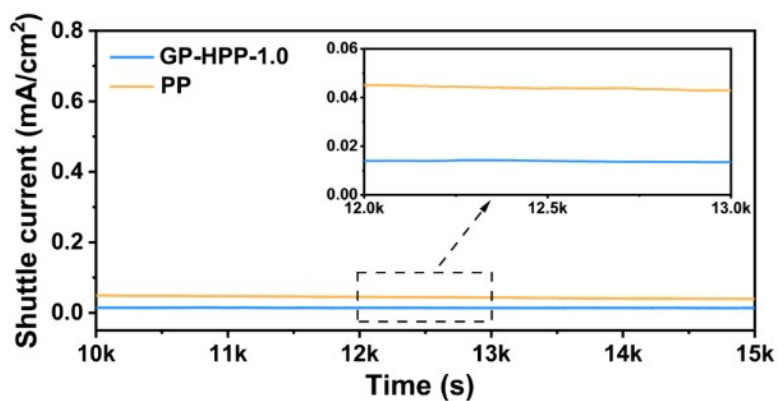
Supplementary Figure 22. The shuttle current tests of PP and GP/HPP-1.0 mL separators.
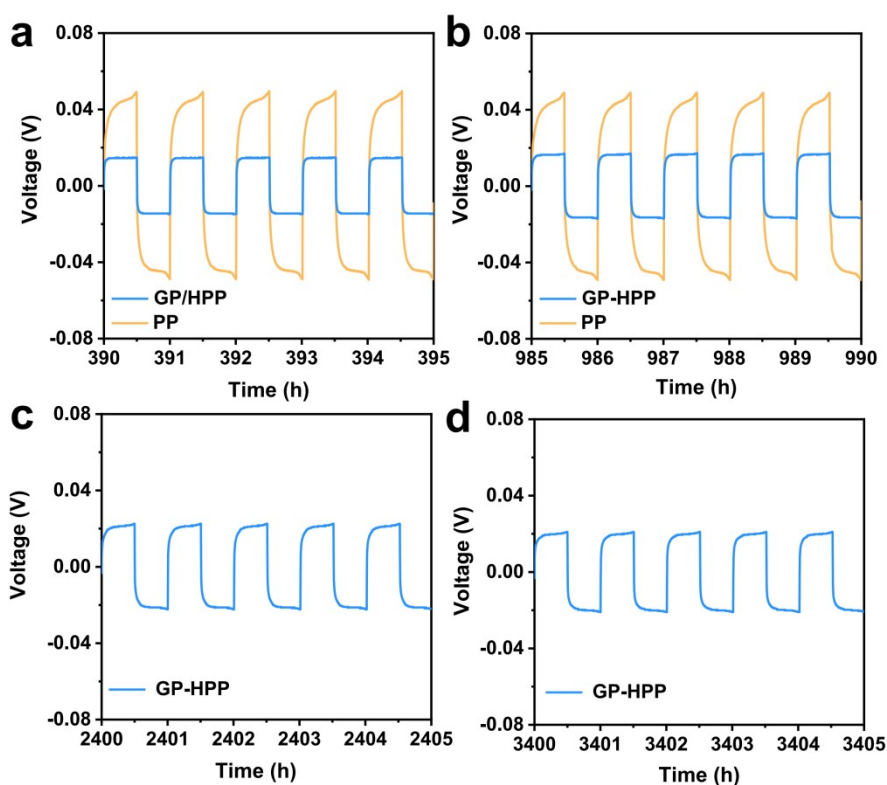
Supplementary Figure 23. Voltage-time profiles of symmetric Li||Li cell with PP and GP/HPP membranes with a capacity of 1 mA h/cm^2 at current density of 2 mA/cm^2 in the cycling interval of (a) 390 to 395 h, (b) 985 to 990 h, (c) 2400 to 2405 h, and (d) 3400 to 3405 h.
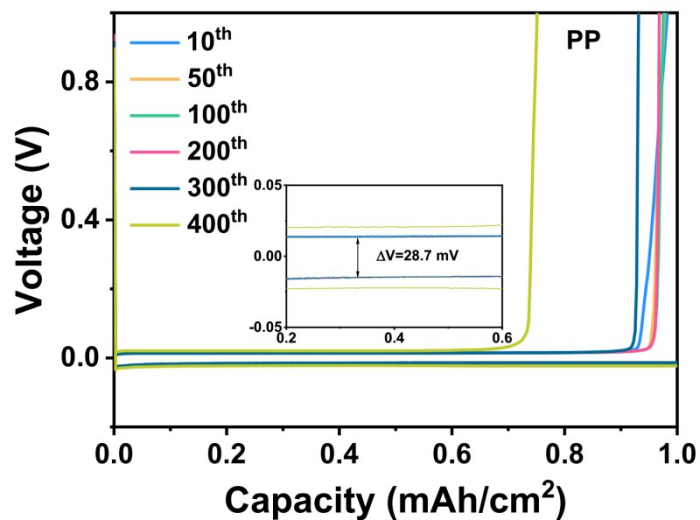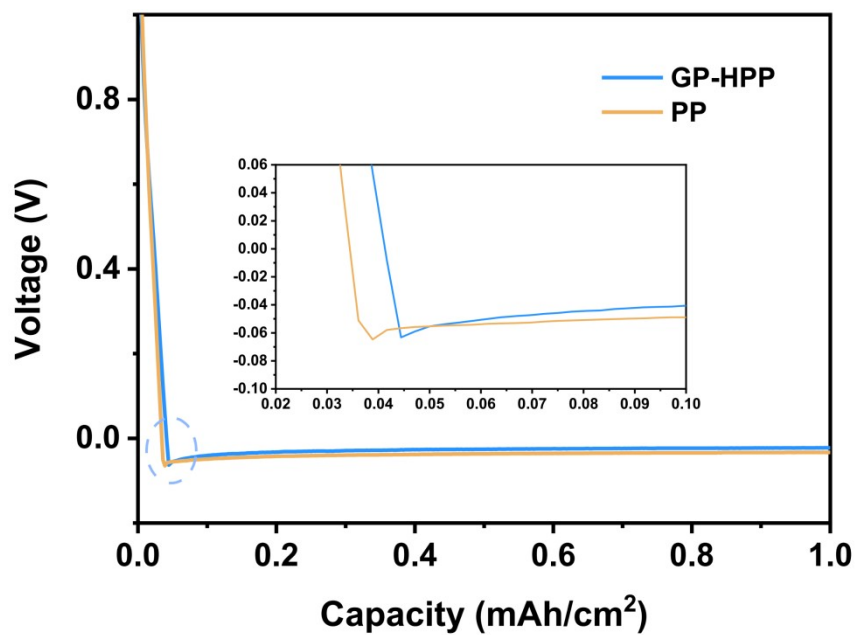
Supplementary Figure 24. The profiles of Li plating/stripping processes in asymmetric Li∥Cu cells with PP separators with a capacity of 1 mAh/cm^2 at 1 mA/cm^2, the insert of the corresponding overpotentials.
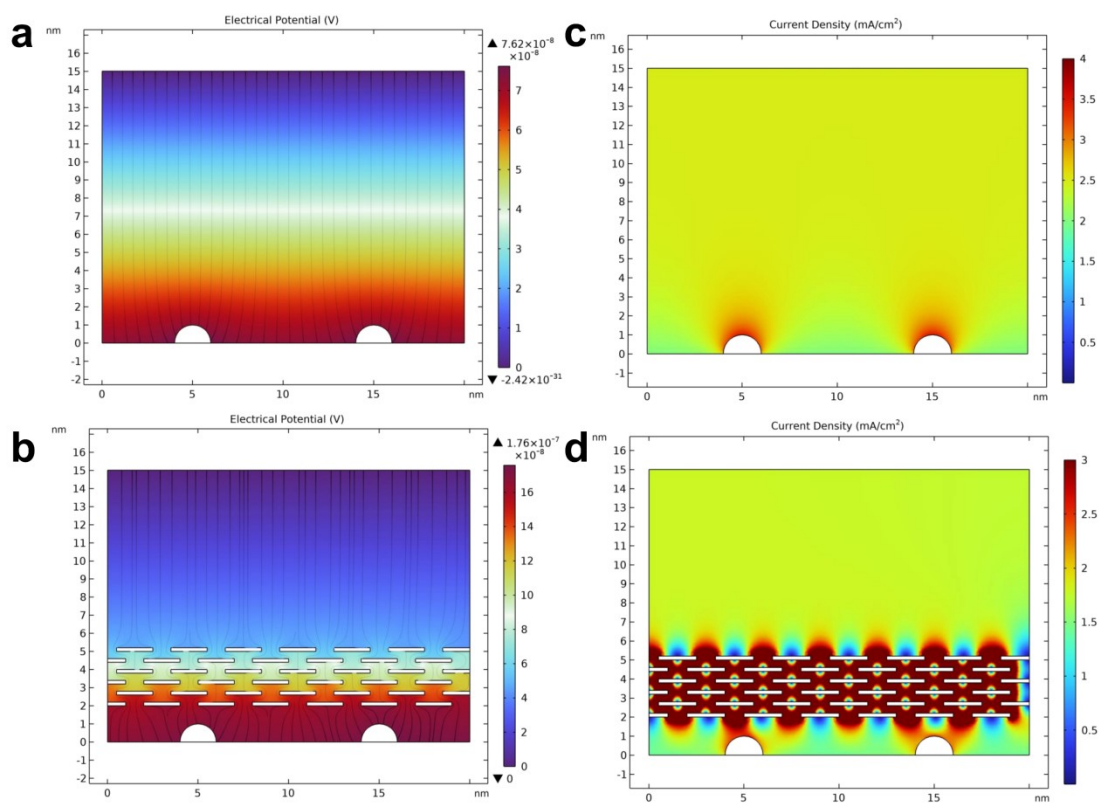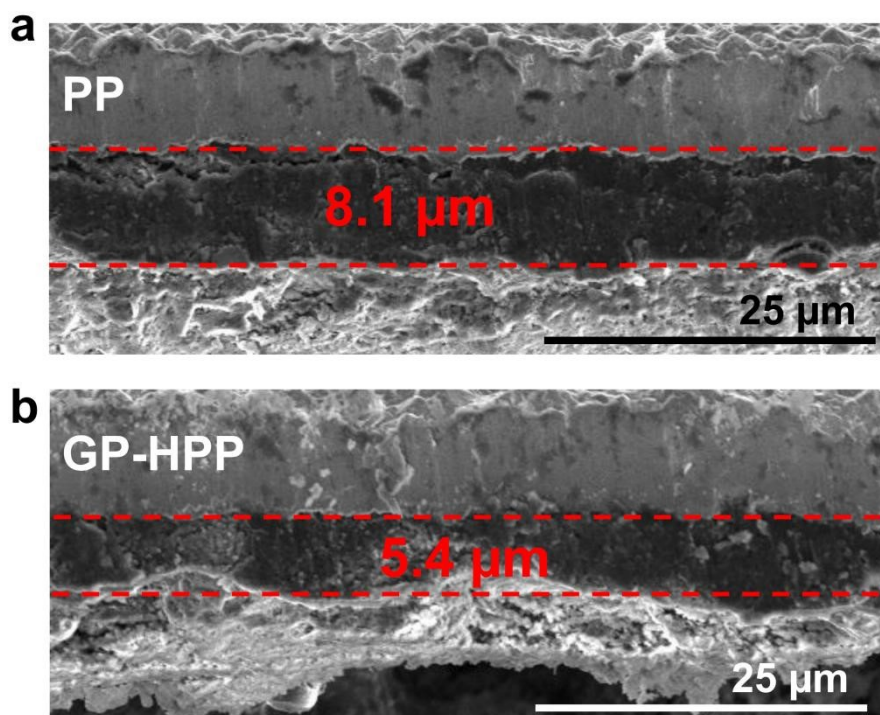

Supplementary Figure 25. Finite element simulations explore the influence of GP/HPP membrane on tuning the distribution of electric potential and the current density.
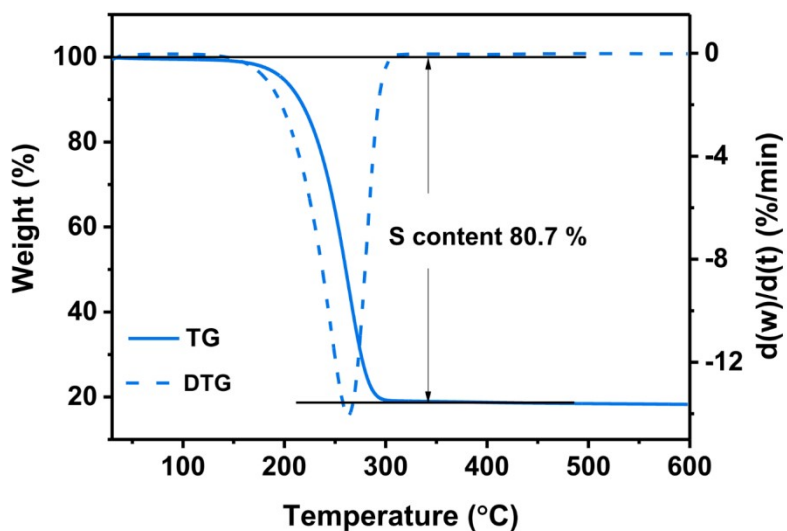
Supplementary Figure 26. Comparison of the corresponding plating/stripping voltage profiles of Li‖Cu half cells with GP/HPP and PP separators.
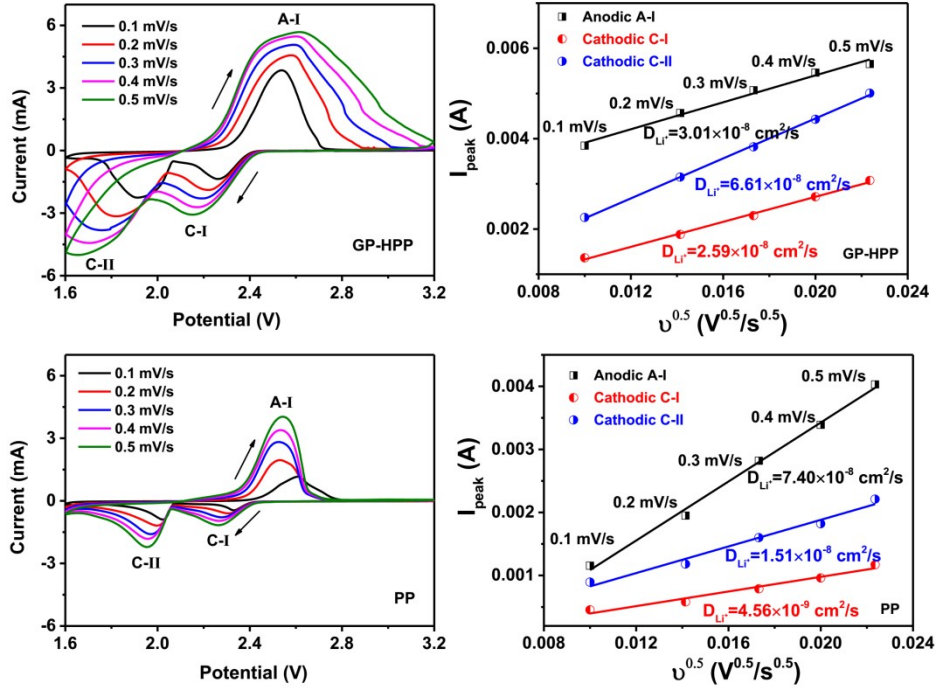

Supplementary Figure 27. The cross-sectional SEM images comparing the lithium deposited thickness of GP/HPP and PP membranes after 100 cycles.

Supplementary Figure 28. Thermogravimetric profiles of Super P-C/S composite.
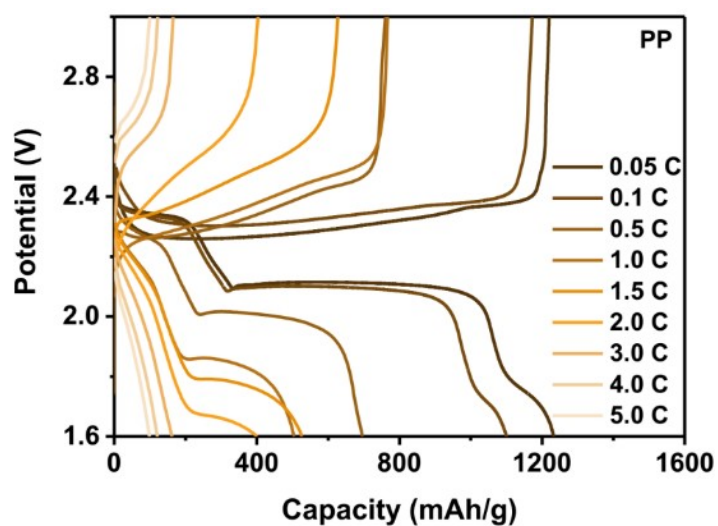
Supplementary Figure 29. The charge/discharge curves of Li-S cells with PP separator at various current densities.
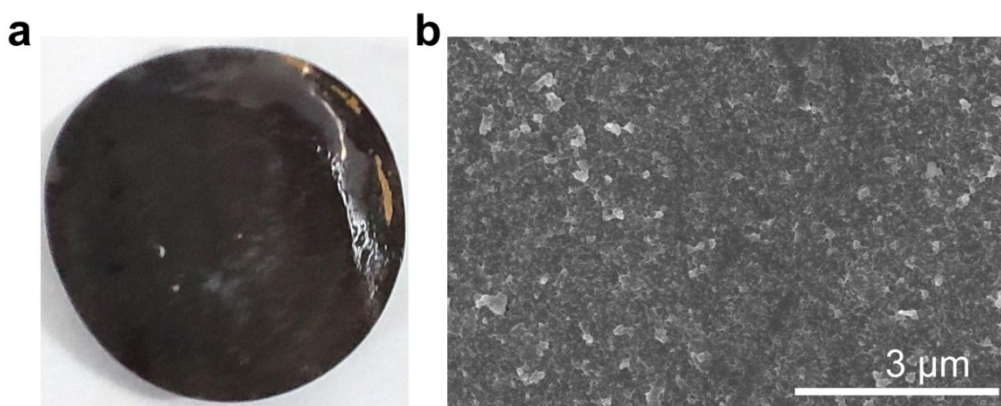
Supplementary Figure 30. CV curves of Li-S cells based on GP/HPP and PP separators at scan rates of 0.1-0.5 mV/s. Linear relationship between the square root of scan rate $v^{0.5}$ and peak current I_{peak} for different cathodic and anodic peak regions.

To investigate the ion diffusion kinetics, the Li^+ diffusion coefficient (D_{Li}^+) was evaluated through CV testing at different scan rates from 0.1-0.5 mV/s. As shown in Fig. S26, with the scan rate increases, the reduction peaks (C-I and C-II) shift to lower potentials and the oxidation peaks (A-I) tend to higher ones. The fast kinetics was confirmed via analyzing these CV curves using the Randles-Sevick equation:

$$I_{peak} = 2.69 \times 10^5 n^{1.5} A D_{Li}^{0.5} v^{0.5} C_{Li}$$

where I_{peak} indicates the peak current (A), n is the number of electrons in the reaction, A is the cathode area (cm^2), v is the scan rate (mV/s), C_{Li} is the Li-ion concentration in the electrolyte. According to this equation, the linear fitting of the plots of peak current (I_{peak}) versus the square root of scanning rate (v) is used to calculate the D_{Li}^+ at the corresponding peak position. The D_{Li}^+ values based on GP/HPP membrane are 3.01×10^{-8} cm^2/s for Peak A-I, 2.59×10^{-8} cm^2/s for Peak C-I, and 6.61×10^{-8} cm^2/s for Peak C-II, respectively. These values are comparable high with PP membrane and exhibit a higher ion diffusion kinetics during the reductive process, indicating that GP/HPP membrane does not obstruct the diffusion of Li^+.

Supplementary Figure 31. (a, b) The optical photograph and SEM image of GP/HPP after the long-term cycling.
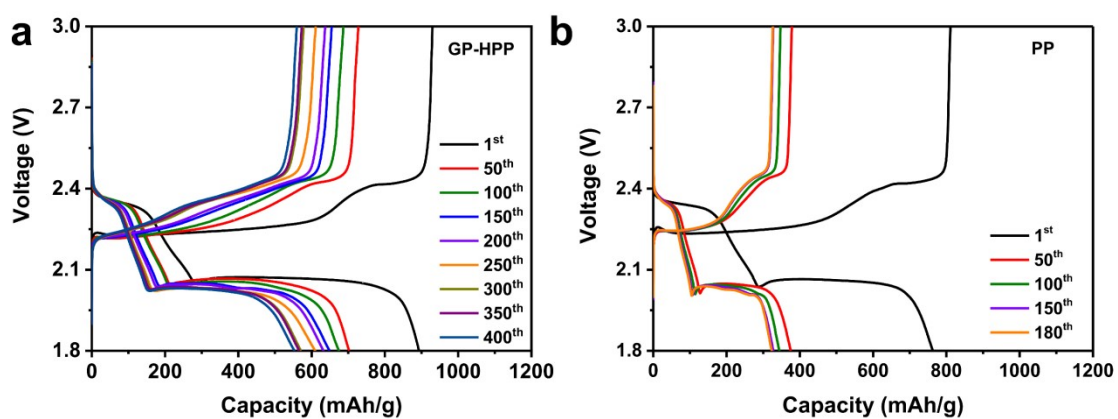
Supplementary Figure 32. The charge/discharge curves at different cycle numbers of Li-S pouch cell with GP/HPP and PP separator.
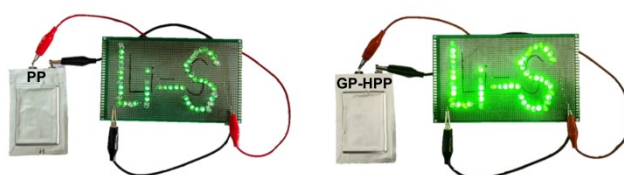
Supplementary Figure 33. Comparison of Li-S pouch cells power LED arrays with GP/HPP and PP separator.

3. Supplementary References (1-12)

1 He, J. et al. High Performance Humidity Fluctuation Sensor for Wearable Devices via a Bioinspired Atomic-Precise Tunable Graphene-Polymer Heterogeneous Sensing Junction. *Chem. Mater.* 2018, **30**, 4343-4354.

2 Xiong, P. *et al.* Atomic-scale regulation of anionic and cationic migration in alkali metal batteries. *Nat. Commun.* 2021, **12**, 4184.

3 Robertson M. J. et al. Development and Testing of the OPLS-AA/M Force Field for RNA. *J. Chem. Theory Comput.* 2019, **15**, 2734-2742.

4 Canongia Lopes J. N. et al. A generic and systematic force field for ionic liquids modeling. *Theor. Chem. Acc.* 2012, **131**, 1-11.

5 Wang C. et al. AUTOFF Program Version 1.0. Hzwtech, Shanghai 2023, see https://cloud. hzwtech. com/web/product-service?id=36.

6 Berendsen H. J. C. et al. Molecular dynamics with coupling to an external bath. *J. Chem. Phys.* 1984, **81**, 3684-3690.

7 Bussi G. et al. Canonical sampling through velocity rescaling. J. Chem. Phys. 2007, **126**, 014101.

8 Darden T. et al. Particle mesh Ewald: An N· log (N) method for Ewald sums in large systems. *J. Chem. Phys*. 1993, **98**, 10089-10092.

9 Wang, L. et al. Covalent bond glued sulfur nanosheet-based cathode integration for long-cycle-life Li-S batteries. *Nano Lett.* 2013, **13**, 6244-6250.

10 Yao, Y. et al. Boosting the Electrochemical Performance of Li-S Batteries with a Dual Polysulfides Confinement Strategy. *Small*. 2018, **14**, 1802516.

11 Hwang, S.-H. et al. Poly(vinyl alcohol) Reinforced and Toughened with Poly(dopamine)-Treated Graphene Oxide, and Its Use for Humidity Sensing. *ACS Nano* 2014, 8, 6739-6747.

12 Pang, Y. et al. Synergetic Protective Effect of the Ultralight MWCNTs/NCQDs Modified Separator for Highly Stable Lithium-Sulfur Batteries. *Adv. Energy Mater.* 2018, 8, 1702288.

13 Liu, Q. T. et al. Dendrite-free and long-cycling lithium metal battery enabled by ultrathin, 2D shield-defensive, and single lithium-ion conducting polymeric membrane. *Adv. Mater.* 2022, 34, 2108437.

14 Wang, J. et al. Hierarchically porous silica membrane as separator for high-performance lithium-ion batteries. *Adv. Mater.* 2022, 34, 2107957.

15 Wang, M. Q. et al. Multifactorial engineering of biomimetic membranes for batteries with multiple high-performance parameters. *Nat. Commun.* 2022, 13, 278.

16 Cao, Y. et al. Ion selective covalent organic framework enabling enhanced electrochemical performance of lithium-sulfur batteries. *Nano Lett.* 2021, 21, 2997-3006.

17 Li, J. et al. Regulate transportation of ions and polysulfides in all-solid-state Li-S batteries using ordered-MOF composite solid electrolyte. *Sci. Adv.* 2024, 10, eadl3925.

18 Wang, W. et al. A sustainable multipurpose separator directed against the shuttle effect of polysulfides for high-performance lithium-sulfur batteries. *Adv. Energy Mater.* 2022, 12, 2200160.

19 Xu, J. et al. Towards high performance Li-S batteries via sulfonate-rich COF-modified separator. *Adv. Mater.* 2021, 33, 2105178.

20 Li, H. Y. et al. An ultrathin functional layer based on porous organic cages for selective ion sieving and lithium-sulfur batteries. *Nano Lett.* 2022, 22, 2030-2037.